

Electrochemistry of Gold Deposition on n-Si(100)

Gerko Oskam^{*,z} and Peter C. Searson^{**}

Department of Materials Science and Engineering, The Johns Hopkins University, Baltimore, Maryland 21218, USA

The electrochemical deposition of gold on n-type silicon from $\text{KAu}(\text{CN})_2$ solutions was investigated by performing a detailed study of the nucleation and growth kinetics. Deposition occurs by progressive nucleation and diffusion-limited growth of three-dimensional hemispherical islands over a wide range of potentials and $\text{KAu}(\text{CN})_2$ concentrations. It is shown that for a silicon/gold electrode, the applied potential is dropped over the silicon/gold interface at potentials more positive than 0 V, while at potentials more negative than 0 V, the applied potential is dropped over the Helmholtz layer at the gold/solution interface. The influence of these observations on the applicability of nucleation models derived for metal-on-metal deposition to metal deposition onto semiconductors is discussed.

© 2000 The Electrochemical Society. S0013-4651(99)07-121-9. All rights reserved.

Manuscript submitted July 30, 1999; revised manuscript received February 14, 2000.

Electrochemical deposition involves charge transfer between a conducting substrate and ions in solution. In metal-on-metal deposition, electrons are transferred from the Fermi energy of the metal into metal ion acceptor states in solution. The Fermi energy in the metal is determined by the potential drop between the solution and the metal. The situation is more complicated for metal deposition on semiconductors since charge transfer can occur via the conduction band, the valence band, or in some cases, via surface states. The positions of the bandedges at the surface and, hence, the energy of surface electrons in the conduction or valence band, are dependent on the partitioning of the applied potential between the semiconductor space-charge layer and the Helmholtz layer at the interface. Analysis of metal deposition at semiconductor surfaces must take these features into account.

Deposition of metals on semiconductors generally occurs by 3D island growth.¹⁻¹¹ For several systems, including Cu on GaAs,^{4,5} Ag,⁶ Au,⁷⁻⁹ Co,¹⁰ Cu,⁸⁻¹⁰ Ni,¹⁰ and Pb¹¹ on Si, it has been shown that deposition follows models for either instantaneous or progressive nucleation and diffusion-limited growth. In this paper we report on the mechanism of nucleation and growth of gold from $\text{KAu}(\text{CN})_2$ solutions on n-type silicon. Current-potential curves indicate that gold is deposited by electron transfer from the conduction band to the solution. Analysis of current transients shows that deposition follows progressive nucleation and diffusion-limited growth over a wide range of concentrations and potentials. From surface imaging it is shown that the nucleus density increases linearly with time up to the current maximum in the deposition transients and remains constant at longer deposition times. Experiments on Si/Au electrodes illustrate the dependence of the potential distribution on applied potential.

Experimental

All experiments were performed on (100) n-type silicon (Wacker Siltronic, AG) with a resistivity of $3 \Omega \text{ cm}$ ($N_D = 1 \times 10^{15} \text{ cm}^{-3}$). Prior to experiments the samples were sequentially cleaned ultrasonically for 10 min in acetone, ethanol, and water. The water was distilled and deionized (Millipore) and had a resistivity of $18 \text{ M}\Omega \text{ cm}$. The ohmic contact was provided by applying InGa eutectic on the back side of the wafer after treatment in 48% HF for 10 s. The samples were then mounted in a cell with an exposed surface area of 2.8 cm^2 . The Ag/AgCl in 3 M NaCl reference electrode was positioned close to the silicon sample using a Luggin capillary, and the counter electrode consisted of a platinum gauze. All potentials are given with respect to the Ag/AgCl reference (0.195 V vs. SHE). The experiments were performed under ambient conditions.

* Electrochemical Society Student Member.

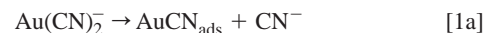
** Electrochemical Society Active Member.

^z E-mail: oskam@jhu.edu

Results and Discussion

Figure 1 shows an energy band diagram for silicon (100) in 1 M KOH. The flatband potential in this solution is -1.1 V (Ag/AgCl),¹²⁻¹⁴ and from the donor density, the position of the conduction band and valence bandedges at the surface are determined to be -1.4 and -0.3 eV , respectively. Since the silicon surface is hydrogen-terminated in 1 M NaOH under open-circuit conditions and at negative potentials,^{12,13} the surface is expected to be hydrogen-terminated during deposition.

The reduction of gold from $\text{Au}(\text{CN})_2^-$ is a two-step reaction involving an adsorbed AuCN intermediate¹⁵⁻¹⁷



For deposition on gold surfaces, AuCN_{ads} is in equilibrium with $\text{Au}(\text{CN})_2^-$ ions in the solution and the charge-transfer step is rate limiting.¹⁵⁻¹⁷ The equilibrium potential, U_{eq} , for the overall reaction is given by

$$U_{\text{eq}} = U_{\text{eq}}^0 + 0.059 \log \frac{[\text{Au}(\text{CN})_2^-]}{[\text{CN}^-]^2} \quad [2]$$

where $U_{\text{eq}}^0 = -0.80 \text{ V}$ (Ag/AgCl).¹⁵⁻¹⁷ From the energy band diagram shown in Fig. 1 it can be seen that the equilibrium potential of the $\text{Au}(\text{CN})_2^-/\text{Au}$ couple is shifted to sufficiently high energy so that deposition is expected to occur via electron transfer from the con-

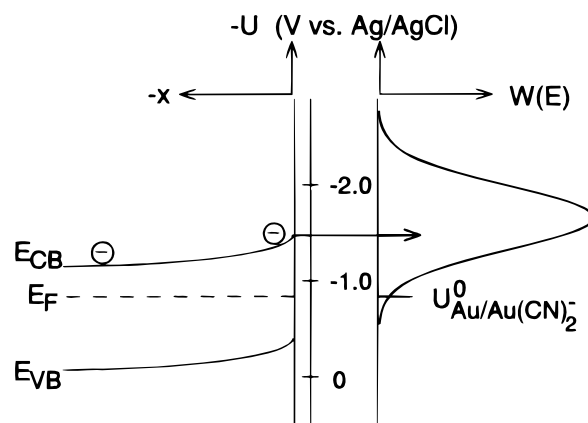


Figure 1. Energy band diagram for n-type silicon (100) in contact with an aqueous solution at pH 14, with the redox couple $\text{Au}/\text{Au}(\text{CN})_2^-$ [only the $\text{Au}(\text{CN})_2^-$ levels are shown]. Gold deposition can be achieved through electron transfer from the conduction band to the solution. Note that there is no overlap between the valence band and the $\text{Au}(\text{CN})_2^-$ levels in solution.

duction band. Since the density of conduction band electrons is determined by the band bending, the deposition process is dependent on the applied potential. Furthermore, by avoiding overlap of the gold ion acceptor states with the valence band, open-circuit (electroless) deposition can be prevented. As a result, the hydrogen-terminated surface is expected to be stable during gold deposition from cyanide solutions.

Current-potential characteristics of silicon.—Figure 2 shows current-potential curves for n-type silicon (100). In KCN solutions, a large cathodic current due to the reduction of water is observed at potentials more negative than about -1.8 V. The cathodic current plateau of about -1.5 mA cm $^{-2}$ in the range from -1.85 to -2 V is related to high cyanide concentrations, and disappears for concentrations lower than 0.1 M KCN. At currents smaller than 1 mA cm $^{-2}$, the current-potential curves are independent of the cyanide concentration, which suggests that the silicon bandedges do not shift as a function of the cyanide concentration in the potential range positive with respect to -1.75 V.

In the solutions containing $\text{KAu}(\text{CN})_2$, reduction of $\text{Au}(\text{CN})_2^-$ is observed in the first scan with an onset at about -1.25 V followed by a current peak of -7.2 mA cm $^{-2}$ at -1.30 V. The observation of a peak in the current-potential curve indicates that the deposition of gold becomes diffusion limited after nucleation has occurred. At about -1.65 V the current increases again due to the reduction of water; the shift in the onset of hydrogen evolution suggests that this reaction occurs preferentially at the gold clusters. The onset of gold deposition in the third and subsequent scans is about 0.2 V more positive than in the first scan indicating that a nucleation overpotential is required for the nucleation of gold islands on the silicon surface.

On the reverse scans a stripping current is not observed indicating that gold deposition on n-type silicon is not reversible. This is caused by two effects: (i) in the dark, the density of holes in the valence band is very low so that the oxidation rate due to valence band holes is low and (ii) the barrier height of the n-Si/Au contact is large (≈ 0.80 eV) so that the rate of thermal excitation of electrons from the gold into the silicon conduction band is very low.

Figure 3 shows current-potential curves for solutions with 2 mM $\text{KAu}(\text{CN})_2 + 1$ M KOH for KCN concentrations from 2 M ($U_{\text{eq}} = -1.01$ V) to 0.02 M ($U_{\text{eq}} = -0.78$ V). It can be seen that the gold deposition peak shifts to more negative potentials with more negative equilibrium potential, while the maximum current is about -0.35 mA cm $^{-2}$ independent of the KCN concentration. The peak current in the 2 mM $\text{KAu}(\text{CN})_2$ solution is a factor 21 smaller than in the 50 mM $\text{KAu}(\text{CN})_2$ solution which shows that the current at the maximum is essentially proportional to the $\text{KAu}(\text{CN})_2$ concentration.

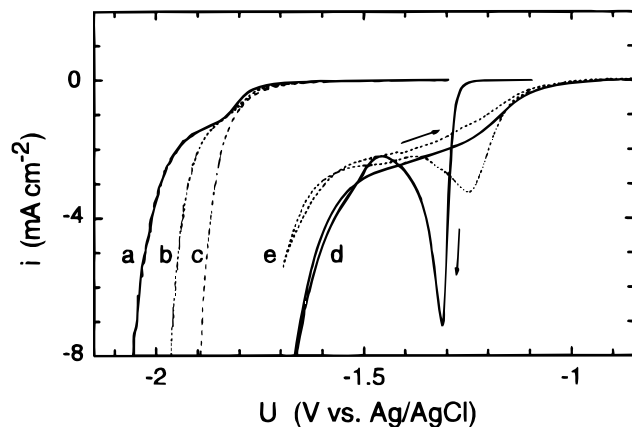


Figure 2. Current-potential curves for n-Si(100) in aqueous solutions at pH 14 with: a, 1 M KCN; b, 0.2 M KCN; and c, 0.008 M KCN. Curves d and e correspond to a 50 mM $\text{KAu}(\text{CN})_2$ solution with 1 M KCN at pH 14. Curve d shows the first scan which was started at -0.85 V, and curve e corresponds to the third scan which represents the final shape of the voltammogram. The scan rate was 10 mV s $^{-1}$ in all cases.

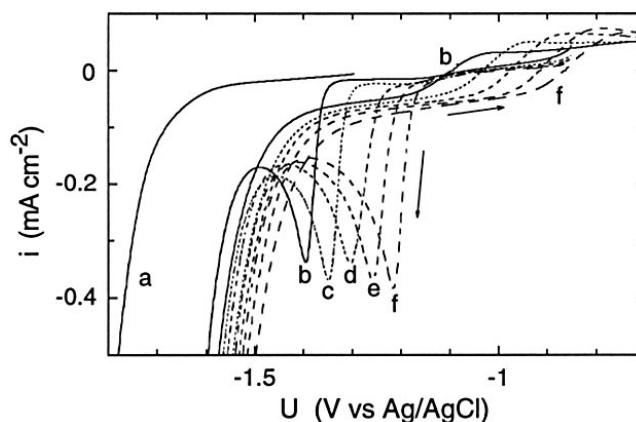


Figure 3. The first scan of current-potential curves for n-Si(100) in 2 mM $\text{KAu}(\text{CN})_2$ solution at pH 14 with b, 2 M KCN; c, 0.6 M KCN; d, 0.2 M KCN; e, 0.06 M KCN; and f, 0.02 M KCN. Curve a shows the current-potential curve for silicon in 0.04 M KCN (pH 14) which is representative for the silicon surface, as the curves for all KCN concentrations overlay in this current regime. The scans were started at OCP, and the scan rate was 10 mV s $^{-1}$.

Figure 4 shows the open-circuit potential (OCP) before the first scan, the potential at the current peak, and the OCP after the first scan vs. the concentration ratio $[\text{Au}(\text{CN})_2^-]/[\text{CN}^-]^2$. The OCP before the first scan is independent of the concentration ratio, indicating that it is not defined by the potential of the gold redox couple, but is controlled by the interaction between the silicon surface and the solution.^{12,13} This result also confirms that nucleation of gold does not take place under open-circuit conditions and is consistent with the observation that a nucleation overpotential is required in order to deposit gold on silicon surfaces. The OCP after the first scan, where approximately 20 equivalent monolayers gold have been deposited, is linear with the concentration ratio with a slope of 59 mV per decade, and is close to the equilibrium potential predicted by Eq. 2.¹⁵ This shows that after gold deposition the open-circuit potential is determined by the $\text{Au}(\text{CN})_2^-/\text{Au}$ couple, however, the reaction is not reversible due to the large energy barrier for gold stripping. The potential at the current maximum is linear with the concentration ratio with a slope of about 43 mV per decade, indicating that the current maximum represents an intermediate case where the current is not completely determined by the energetics of the redox couple.

The potential regime where deposition occurs is more than 0.15 V more negative than the flatband potential, indicating that the

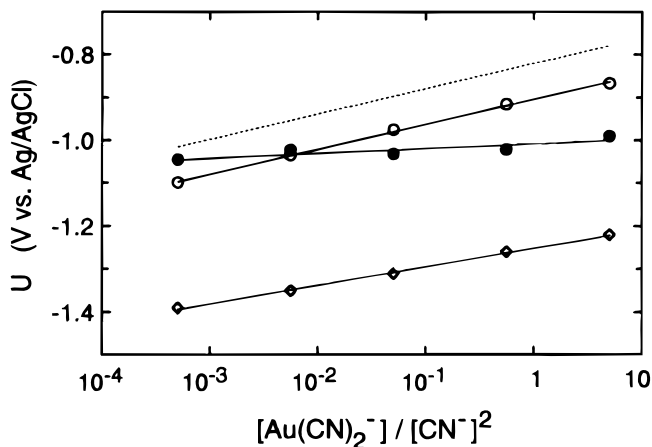


Figure 4. The equilibrium redox potential (.....), the open-circuit potential before the first scan (●), the peak potential in the first scan (◇), and the open-circuit potential after the first scan (○) for n-Si(100) in the 2 mM $\text{KAu}(\text{CN})_2$ solutions at pH 14 at the same KCN concentrations as in Fig. 3 vs. the concentration ratio $[\text{Au}(\text{CN})_2^-]/[\text{CN}^-]^2$.

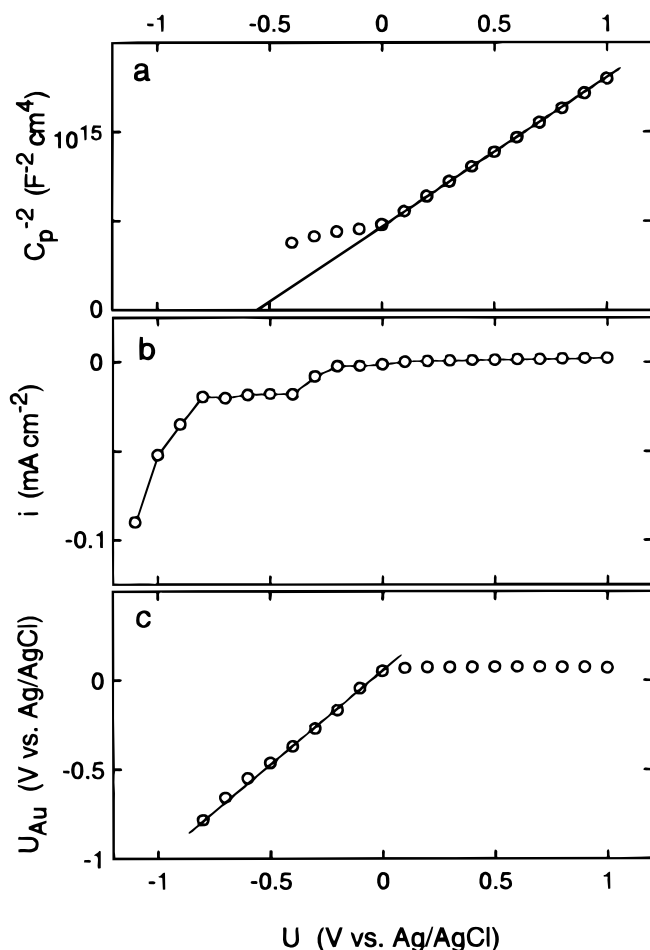


Figure 5. Simultaneous experiments on a silicon electrode covered with a continuous, 150 nm gold film in a 0.1 M $\text{K}_4\text{Fe}(\text{CN})_6$ + 0.5 M KCl solution: (a) steady-state current-potential curve, (b) Mott-Schottky plot [frequency = 10 kHz; amplitude = 5 mV (rms)], (c) the potential of the gold film with respect to the reference electrode vs. the applied potential.

silicon surface is in weak accumulation. In accumulation, the capacitance of the silicon space-charge layer becomes comparable to that of the Helmholtz layer^{18,19} and the bandedges become unpinning. Under these conditions, most of the applied potential will be dropped across the Helmholtz layer. This situation is comparable to metal-on-metal deposition where the applied potential is dropped across the Helmholtz layer resulting in a change of the overpotential for the deposition reaction.

Current-potential characteristics of gold-covered silicon electrodes.—The electrochemical nucleation and growth of gold onto silicon is complicated by the presence of three interfaces: silicon/electrolyte, silicon/gold, and gold/electrolyte. In order to determine the potential distribution at the silicon/gold/electrolyte interfaces, experiments were performed on silicon with a 150 nm continuous gold film where the potential of the gold film was monitored as a function of the potential applied to the silicon.^{20,21}

Figure 5 shows the Mott-Schottky plot, the current-potential curve, and the potential of the gold layer vs. the applied potential in a solution of 0.1 M $\text{K}_4\text{Fe}(\text{CN})_6$ + 0.5 M KCl at pH 9. At potentials more positive than 0 V, the Mott-Schottky plot is linear and the flat-band potential is -0.54 V, close to the value for the silicon surface.^{22,23} This result shows that in this potential range the applied potential is dropped over the silicon space-charge layer which implies that the potential drop over the gold/electrolyte solution interface remains constant. This is corroborated by Fig. 5c which shows that the potential of the gold layer is about 0.07 V, corresponding to the redox potential of the $\text{Fe}(\text{CN})_6^{3-/4-}$ couple, independent of the potential applied to the silicon.

In the potential region more negative than 0 V the capacitance-potential plot shows a plateau indicating that the band bending does not change with the applied potential. In this region, the potential of the gold layer changes linearly with the applied potential with a slope close to 1 as shown in Fig. 5c. At sufficiently negative potentials the cathodic current is due to the reduction of water; the small current plateau of $17 \mu\text{A cm}^{-2}$ is due to reduction of $\text{Fe}(\text{CN})_6^{3-}$.

These results are summarized in the energy band diagrams shown in Fig. 6. At positive potentials (Fig. 6c) the silicon surface is in depletion and any change in the applied potential leads to a change of the band bending. As a result, the potential drop across the Helmholtz layer remains constant. The small anodic current is related to the excitation of electrons from the gold Fermi energy to the silicon conduction band, and is close to the saturation current of $3 \times 10^{-7} \text{ A cm}^{-2}$ for a Si/Au Schottky junction with a 0.80 eV barrier height.²⁴ Since the exchange current for the redox couple is much larger than the saturation current, the potential of the gold layer is pinned at the equilibrium potential of the redox couple.

At about 0 V, the silicon Fermi level is aligned with that of the gold layer (Fig. 6b). At this potential, the band bending is equal to the built-in potential of the Si/Au Schottky junction. From the Mott-Schottky plot the band bending at 0 V is determined to be 0.54 eV. Since the silicon Fermi energy is 0.27 eV below the conduction band (in the bulk), the barrier height, which corresponds to the energy difference between the conduction bandedge at the surface and the gold Fermi energy, is 0.81 eV in good agreement with measurements on dry Si/Au junctions and published values.^{7,24}

At negative potentials (Fig. 6a), the forward current from the silicon to the gold becomes larger than the exchange current of the redox couple, and the gold Fermi energy becomes unpinning from that of the

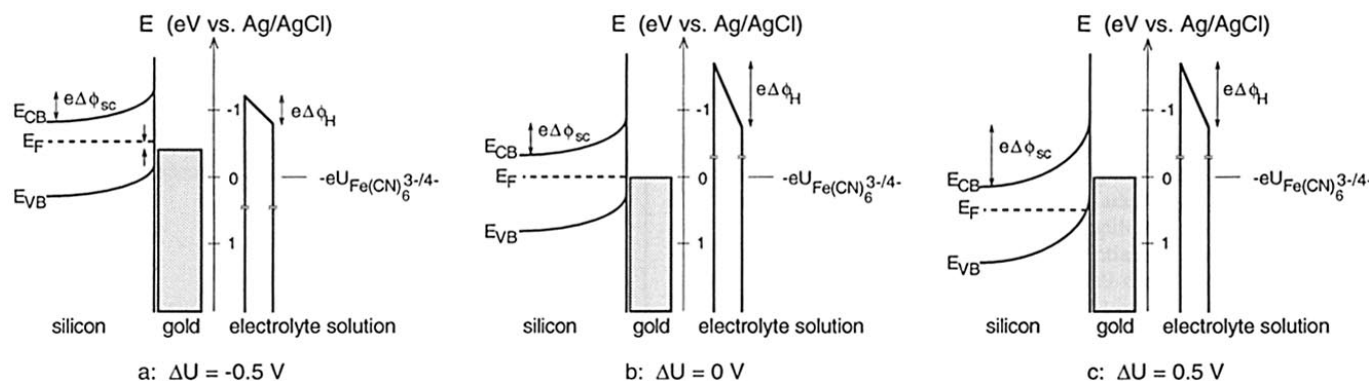


Figure 6. Band diagrams at three potentials for electrodes consisting of n-type silicon covered with a 150 nm continuous gold film in 0.1 M $\text{K}_4\text{Fe}(\text{CN})_6$ + 1 M KCl solution at pH 9. The electrostatic potential drops across the silicon space-charge layer and the Helmholtz layer at the gold surface are indicated as $\Delta\phi_{sc}$ and $\Delta\phi_H$, respectively. Note that the widths of the space-charge and Helmholtz layers are not to scale.

solution. For a cathodic current to flow, the Fermi energies of the silicon and the gold must be above the Fermi energy of the redox couple. To achieve a current of $17 \mu\text{A cm}^{-2}$, a forward bias across the Si/Au interface of about 0.1 V (for an ideality factor of 1) is needed. Thus, as the applied potential is shifted from 0 to -1 V, most of the applied potential is dropped over the Helmholtz layer and the Fermi energy of the gold remains close to that of the silicon.

Time dependence of nucleation and growth.—The mechanism of nucleation and growth was determined from current transients.²⁵⁻³⁶ The density of nuclei as a function of time at a constant potential, $N(t)$, can be described in terms of a nucleation rate constant, k

$$N(t) = N_0 \{1 - \exp(-kt)\} \quad [3]$$

where N_0 is the final nucleus density. From Eq. 3 two limiting cases can be identified. If k is large and $kt \gg 1$ at short times then $N(t) = N_0$. Conversely, if k is small and $kt \ll 1$ at short times then $N(t) = kN_0t$, and the density of nuclei increases linearly with time. The first case corresponds to instantaneous nucleation and the second case corresponds to progressive nucleation.

The growth of nuclei can be either kinetically limited, diffusion limited, or under mixed control. From Fig. 2 and 3 it was inferred that growth is diffusion limited at potentials more negative than the current peak. As growth becomes diffusion limited, the diffusion zones around individual nuclei start to overlap, and linear diffusion to the planar surface can occur before nuclei impinge on each other.

Figure 7 shows the nucleus density as a function of time for gold deposition at -1.30 V. Nuclei were formed by stepping the potential to -1.30 V for different times, and subsequently growing them at -1.10 V where the nucleation rate is negligible. The total deposition charge was 3.0 mC cm^{-2} for all samples, corresponding to 13.5 equivalent monolayers of gold. From Fig. 7 it can be seen that at times shorter than about 0.9 s the nucleus density increases linearly with time, corresponding to progressive nucleation. At longer times, the nucleus density becomes independent of time indicating that either all nucleation sites have been occupied or that remaining nucleation sites have been screened by the expanding diffusion fields around existing nuclei.

The time dependent deposition current density (normalized to the geometric surface area), $i(t)$, for progressive nucleation followed by three-dimensional diffusion-limited growth is²⁷⁻²⁹

$$i(t) = \frac{zFD^{1/2}c}{\pi^{1/2}t^{1/2}} \left[1 - \exp\left(-\frac{2}{3}kN_0\pi Dt^2(8\pi cV_m)^{1/2}\right) \right] \quad [4]$$

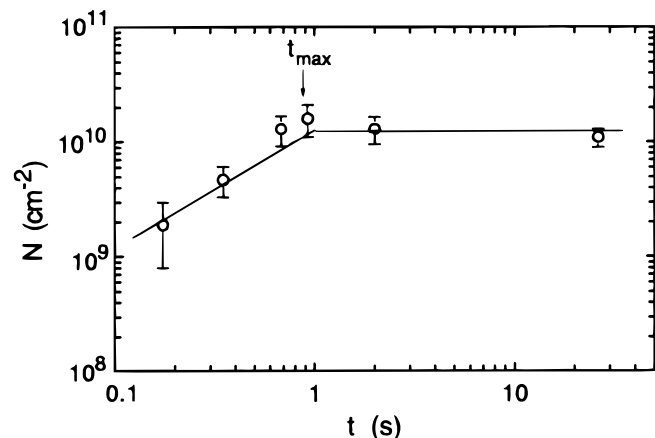


Figure 7. The nucleus density as a function of the pulse length for deposition at -1.30 V from $2 \text{ mM KAu(CN)}_2 + 0.2 \text{ M KCN}$ (pH 14), determined using SEM. The nuclei were grown at -1.10 V after the nucleation pulse so that the deposition charge was -3.0 mC cm^{-2} in all cases. The time of the current maximum in the transient is indicated.

where D is the diffusion coefficient, c is the metal ion concentration in the bulk solution, and V_m is the molar volume of the metal. The current initially increases with time due to 3D diffusion to an increasing metal surface area, and then decreases as the diffusion zones around the growing nuclei start to overlap resulting in a 1D diffusion-limited current to a planar surface.

Figure 8 shows current transients for potential steps from the open-circuit potential to various deposition potentials for the $2 \text{ mM KAu(CN)}_2 + 0.2 \text{ M KCN}$ (pH 14) solution. At long times, the transients in the range from -1.55 to -1.35 V all converge on a decay curve governed by linear diffusion to a planar surface according to the Cottrell equation. At -1.65 V and -1.60 V, the current after the maximum is significantly higher due to co-reduction of water to hydrogen. This can be seen from the current-potential curve shown in Fig. 3 (curve d) where the onset of hydrogen evolution on a partly gold-covered surface is observed at about -1.55 V.

The nucleation mechanism can be determined by comparing the normalized current transients to theoretical models. For progressive nucleation and diffusion limited growth we can rewrite Eq. 4 in terms of the maximum current, i_{max} , and the time at which the maximum current is observed, t_{max} ²⁷⁻²⁹

$$\frac{i^2}{i_{\text{max}}^2} = 1.2254 \left(\frac{t_{\text{max}}}{t} \right) \left[1 - \exp\left(-2.3367 \frac{t^2}{t_{\text{max}}^2}\right) \right]^2 \quad [5]$$

The time in Eq. 4 and 5 represents the time with respect to the onset of the deposition current, *i.e.*, t is corrected for the induction time, t_0 . The induction time may be considered as the time required to form a stable nucleus. The induction time was determined by extrapolation of the current rise to a deposition current of zero, and $t_0 < 0.1t_{\text{max}}$ in all cases.

Figure 9 shows the reduced parameter plots for the transients at -1.29 , -1.45 , -1.55 , and -1.65 V. The theoretical curves for progressive nucleation (solid line) and instantaneous nucleation (dotted line) and diffusion-limited growth are also shown. The transient at -1.65 V agrees with the progressive nucleation model before the maximum. After the maximum, the current is increased due to simultaneous reduction of water which only becomes significant after the gold clusters have grown to a sufficient size. In the potential range from -1.40 to -1.55 V, the plots agree very well with the progressive nucleation and growth model. At potentials more positive than -1.35 V, the experimental results deviate from the progressive nucleation and diffusion-limited growth model at longer times. This is due to mixed charge transfer/mass transport control, consistent with the current-potential curve shown in Fig. 3 (curve d) where growth of the clusters is partly kinetically limited at potentials more positive than about -1.32 V.

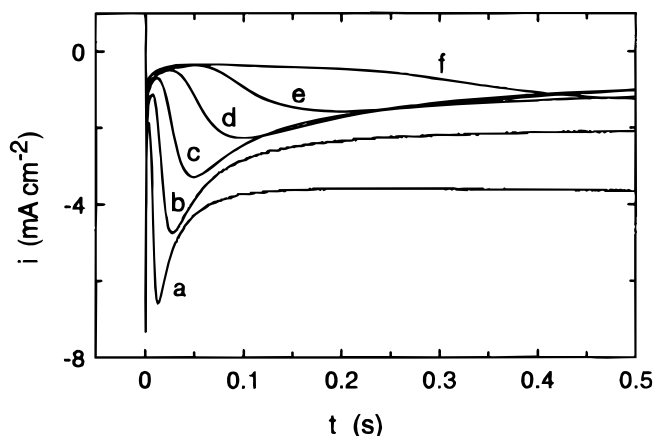


Figure 8. Current transients in 2 mM KAu(CN)_2 with 0.2 M KCN at pH 14 for potential steps from the open-circuit potential to: a, -1.65 V; b, -1.60 V; c, -1.55 V; d, -1.50 V; e, -1.45 V; and f, -1.40 V.

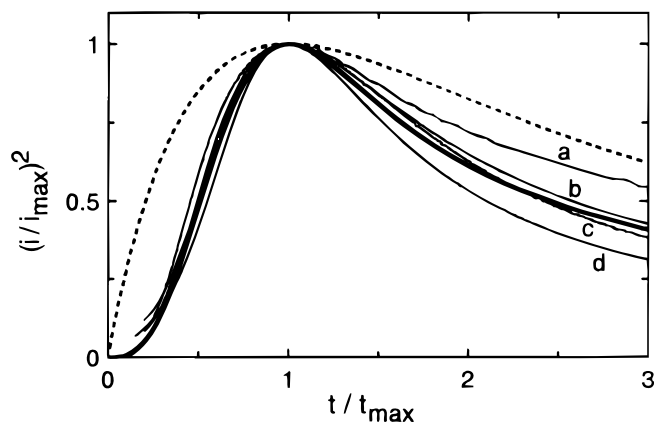


Figure 9. Dimensionless plots of the current transients from Fig. 5 at a, -1.65 V; b, -1.55 V; c, -1.45 V; and d, -1.29 V. The bold solid line corresponds to the calculated curve for progressive nucleation and diffusion-limited growth, and the bold dotted line represents the theoretical curve for instantaneous nucleation and diffusion-limited growth.

Current transients were also recorded for solutions with 50, 10, and 0.5 mM $\text{KAu}(\text{CN})_2$. Analysis showed that in all cases gold deposition proceeds through progressive nucleation and diffusion-limited growth. Figure 10 shows the time and current at the maximum vs. the deposition potential. The values for t_{max} and i_{max} are exponentially dependent on the deposition potential with inverse slopes of 166 mV per decade and -325 mV per decade, respectively, in the potential range between about -1.35 to -1.70 V. At potentials more positive than -1.35 V, the curves for t_{max} and i_{max} vs. potential have a higher slope. Using Eq. 4 for progressive nucleation and diffusion-limited growth, the following relations can be derived for these parameters

$$t_{\text{max}} = 3.318D^{-1/2}c^{-1/4}(8\pi V_m)^{-1/4}(kN_0)^{-1/2} \quad [6]$$

$$i_{\text{max}} = 0.4959zFD^{3/4}c^{9/8}(8\pi V_m)^{1/8}(kN_0)^{1/4} \quad [7]$$

If it is assumed that only the nucleation rate kN_0 is potential dependent, differentiation of Eq. 6 and 7 leads to $\delta U/\delta[\log(i_{\text{max}})] = -2 \delta U/\delta[\log(t_{\text{max}})]$, which is in good agreement with the results in Fig. 10 where $\delta U/\delta[\log(i_{\text{max}})] = -1.96 \delta U/\delta[\log(t_{\text{max}})]$.

Figure 10 shows that t_{max} is weakly dependent on the $\text{KAu}(\text{CN})_2$ concentration while i_{max} is strongly dependent on concentration. From Eq. 6 and 7 note that t_{max} is expected to be proportional to $c^{-1/4}$, while i_{max} should be proportional to $c^{9/8}$. The inset of Fig. 10b shows a power-law dependence of i_{max} on c . A least squares fit resulted in a slope of 1.08, very close to the expected value of $9/8$. The concentration dependence of t_{max} could not be verified due to the weak dependence.

The diffusion coefficient can be obtained from the deposition transients using Eq. 6 and 7. From the product $t_{\text{max}} i_{\text{max}}^2$, D was determined to be $1.5 \times 10^{-5} \text{ cm}^2 \text{ s}^{-1}$ in the 50 mM $\text{KAu}(\text{CN})_2$ solution which is in good agreement with values reported previously for dilute solutions.¹⁶ The diffusion coefficient exhibited a weak concentration dependence, suggesting that at lower concentrations the current efficiency for gold deposition is lower due to the co-reduction of water.

These results show that the deposition of gold on silicon follows the progressive nucleation and diffusion-limited growth model that was derived for metal-on-metal deposition assuming that the applied potential is dropped across the Helmholtz layer. Note that at $t = 0$, the silicon surface is not in equilibrium with the $\text{Au}(\text{CN})_2^-/\text{Au}$ redox couple, while at $t \approx 3t_{\text{max}}$, where the silicon surface is partly covered with gold, the electrode acts as a gold electrode. However, the equilibration process does not appear to result in a significant deviation from the theoretical model. In addition, Fig. 7 shows that the nucleation process stops at about t_{max} and, hence, the assumption that $N(t) = kN_0t$ is no longer valid. However, for $t \geq 1.13 t_{\text{max}}$ the total current $\geq 95\%$ of the 1D diffusional current so that the formation of

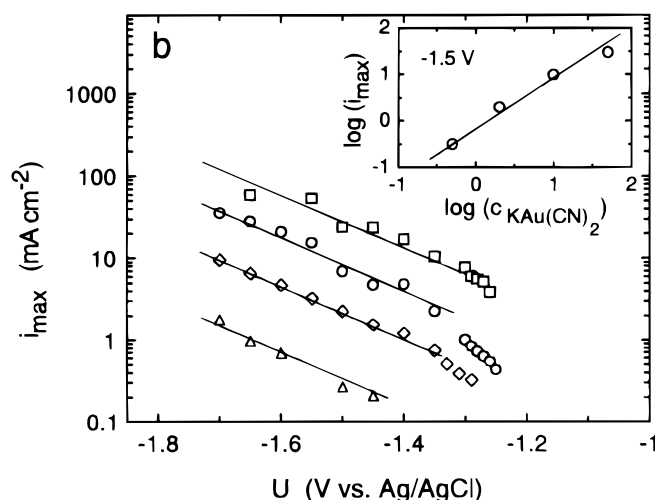
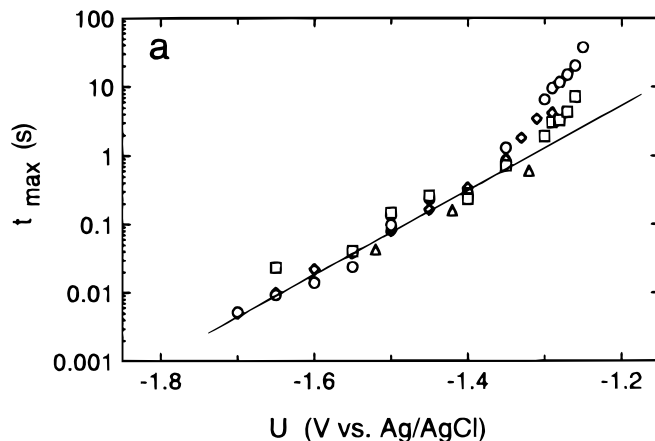


Figure 10. Transient analysis for experiments in four concentrations of $\text{KAu}(\text{CN})_2$: (□) 50 mM $\text{KAu}(\text{CN})_2 + 1$ M KCN (pH 14), (○) 10 mM $\text{KAu}(\text{CN})_2 + 1$ M KCN (pH 14), (◇) 2 mM $\text{KAu}(\text{CN})_2 + 0.2$ M KCN, and (△) 0.5 mM $\text{KAu}(\text{CN})_2 + 0.5$ M KCN (pH 14). (a) The time at the current maximum (corrected for the induction time) and (b) the current at the maximum vs. the applied potential. The inset shows the current maximum at -1.50 V vs. the concentration on a logarithmic scale; the solid line represents a slope of $9/8$.

additional nuclei cannot lead to a significant increase in current, although it may result in a redirection of the ion flux.

Potential and concentration dependence of the nucleation rate.—For progressive nucleation, the nucleation rate is given by $J_{\text{nucl}} = dN(t)/dt = kN_0$. The nucleation rate can be obtained from the maximum in the current transients using the following relation (see Eq. 6 and 7)

$$J_{\text{nucl}} = kN_0 = 0.2898(8\pi c V_m)^{-1/2} \frac{(zFc)^2}{i_{\text{max}}^2 t_{\text{max}}^3} \quad [8]$$

Figure 11 shows $\log(kN_0)$ vs. potential for $\text{KAu}(\text{CN})_2$ concentrations ranging from 0.5 to 50 mM. The relationship is linear between -1.4 and -1.7 V, and essentially independent of the concentration. The inverse slope in this potential region is -78 mV per decade. In the potential range positive of -1.40 V, the inverse slope is about -21 mV per decade.

The potential dependence of the nucleation rate can be analyzed by comparison to models for nucleation and growth.^{26,37-44} In the kinetic approach, the formation of a cluster is treated as a sequence of attachment and detachment steps. In equilibrium, the attachment and detachment rates are equal, whereas supersaturation leads to an

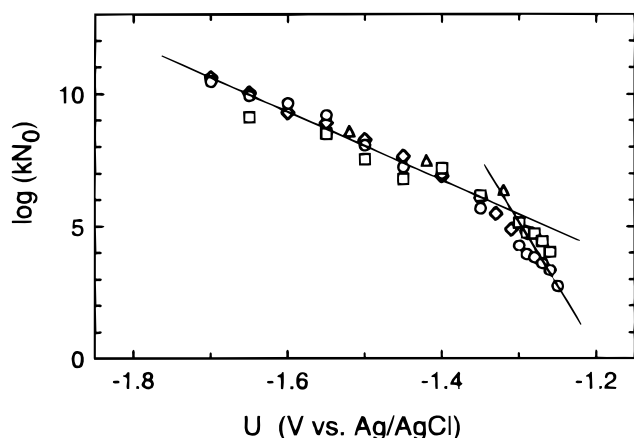


Figure 11. The logarithm of the nucleation rate, kN_0 , vs. the applied potential for the same solutions as in Fig. 7, represented by the same symbols.

increase in the attachment rate and growth of the cluster. The nucleation rate, J_{nucl} , is given by²⁶

$$J_{\text{nucl}} = A_{3D}^* \exp\left(\frac{\beta e|\eta|}{kT}\right) \exp\left(\frac{N_{\text{crit}} e|\eta|}{kT}\right) \quad [9]$$

where N_{crit} is the number of atoms required to form a critical nucleus, and η is the overpotential. The pre-exponential factor A_{3D}^* is independent of potential as long as N_{crit} is potential independent, and the factor β depends on the mechanism of attachment. Equation 9 reduces to the Volmer-Weber model for nucleation if $N_{\text{crit}} \gg \beta$. The total potential dependence of the nucleation rate in a potential range where N_{crit} is constant is thus given by

$$\frac{d \log(J_{\text{nucl}})}{d|\eta|} = \frac{e}{2.303kT} (\beta + N_{\text{crit}}) \quad [10]$$

The value of β in Eq. 9 and 10 results from the attachment probability of the atom converting a cluster into a stable nucleus. If the attachment occurs through direct transfer of metal ions to the cluster and simultaneous charge transfer then $\beta = \alpha_c$ where α_c is the cathodic charge-transfer coefficient. If the mechanism is attachment of adatoms to the cluster, then the potential dependence of the adatom concentration yields $\beta = 1$.^{26,36} Note that in order to apply Eq. 10 to the case of metal deposition onto a semiconductor surface, the overpotential needs to be defined as a function of the applied potential. Since the deposition potentials are negative of the flatband potential, we assume that any change in the applied potential is dropped across the Helmholtz layer so that the overpotential is proportional to the applied potential ($|\eta| = |U| + \text{const}$).⁴

From Fig. 11 we obtain an inverse slope of -78 mV per decade in the potential range between -1.4 and -1.7 V, which gives a value for N_{crit} of about 0 assuming that β is between 0.5 and 1. This result suggests that an adsorbed gold atom can be considered as a stable cluster⁴⁴ in this potential range. Since the barrier for dissolution of gold atoms is very large the attachment/detachment process is highly irreversible, consistent with $N_{\text{crit}} \leq 1$. In the potential range positive of -1.40 V, the inverse slope of the curve is about -21 mV per decade, which leads to $N_{\text{crit}} \approx 2$. Note that N_{crit} is expected to increase with decreasing driving force, *i.e.*, with less negative potential.²⁶ Note that the applied potential in these experiments was always greater than 200 mV more negative than the equilibrium potential of the $\text{Au}(\text{CN})_2^-/\text{Au}$ redox couple. Similar values for N_{crit} at potentials sufficiently negative of the equilibrium potential have been reported for copper deposition on GaAs,^{4,5} as well as for metal-on-metal deposition (*e.g.*, Ref. 26). For the system n-Si(111)/ Pb^{2+} , a value of $N_{\text{crit}} = 11$ was obtained at potentials close to the redox potential ($|U - U_{\text{redox}}| < 15$ mV).¹¹

Figure 12 shows the potential dependence of the nucleus density for deposition from 50 and 2 mM $\text{KAu}(\text{CN})_2$ solutions determined from scanning electron microscopy (SEM) and atomic force microscopy (AFM) images. At potentials more negative than about -1.30 V the nucleus density is independent of potential indicating that the potential dependence of the nucleation rate kN_0 , as shown in Fig. 11, is determined by the potential dependence of k . At potentials more positive than about -1.30 V, the nucleus density decreases, indicating that the larger slope in the $\log(kN_0)$ vs. potential plot is due to the potential dependence of N_0 . The observation that the nucleus density is potential dependent suggests the presence of active sites with different activation energies for nucleation.

Figure 12 also shows the nucleus density for the two solutions estimated from the transients assuming that the nucleus density reaches its maximum value at t_{max} , as was observed for deposition at -1.30 V (see Fig. 7). Using Eq. 3 we can then write $N(t = t_{\text{max}}) = kN_0 t_{\text{max}}$. From Fig. 12 it can be seen that the nucleus density from imaging techniques is larger than the value obtained from analysis of the transients, and that the magnitude of the deviation is potential dependent. Similarly, the nucleation rate can be estimated from the SEM and AFM results, and compared to the values for kN_0 obtained from the transients. In this case, the potential dependence of kN_0 from SEM and AFM is found to be much weaker than that obtained from the transients. As a consequence, calculation of the critical nucleus size using Eq. 10 would lead to $N_{\text{crit}} = 0$ over the entire potential regime.

The reason for the large discrepancy between the observed nucleus densities and those estimated from current transients is not clear. A possible explanation is that the time and current at the maximum

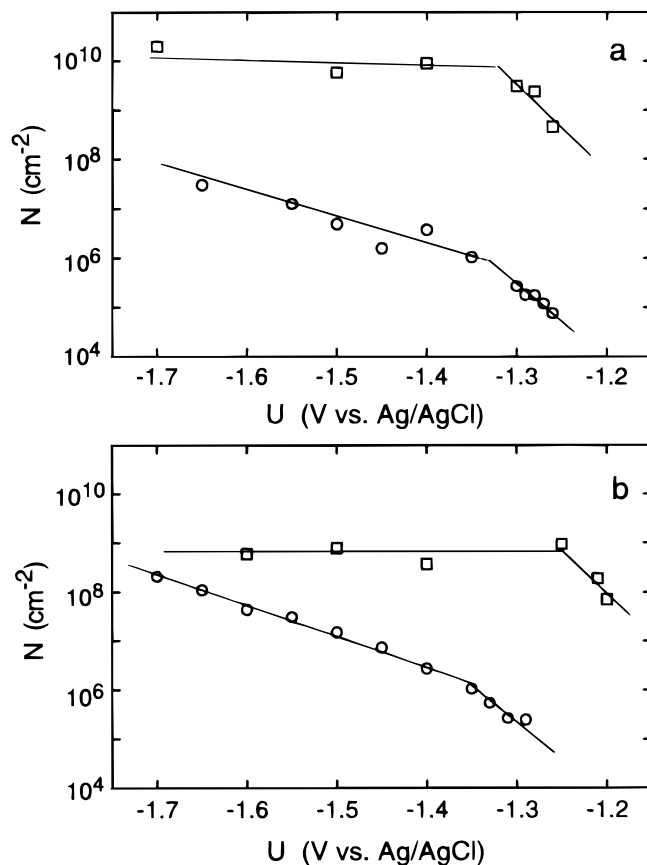


Figure 12. The nucleus density vs. the applied potential for deposition from imaging techniques and estimated from current transients using $N = kN_0 t_{\text{max}}$ for (a) 50 mM $\text{KAu}(\text{CN})_2 + 1$ M KCN (pH 14); the nucleus density was determined from SEM (\square) and estimated from transients (\circ). (b) 2 mM $\text{KAu}(\text{CN})_2 + 0.2$ M KCN (pH 14); the nucleus density was determined from AFM (\square) and estimated from transients (\circ).

do not accurately describe the time of overlap of the diffusion zones of individual nuclei. The radius of the diffusion field to an isolated nucleus is $r_d = (8\pi cV_m)^{1/4} D^{1/2} t^{1/2}$. Thus, the time at which the diffusion zones begin to overlap can be estimated from $t_{\max} = r_d^2(t_{\max}) D^{-1} (8\pi cV_m)^{-1/2} \approx (4N_0)^{-1} D^{-1} (8\pi cV_m)^{-1/2}$. For example, the time needed to reach overlap of diffusion zones for a nucleus density of 10^{10} cm^{-2} is expected to be on the order of 50 μs (using $c = 10 \text{ mM}$). However, the values for t_{\max} were typically 10 ms to 1 s. Hence, the current maximum may be related to the diffusion of ions to multiple nuclei and the overlap of the cluster diffusion zones, instead of those of individual nuclei. As a consequence, the value of kN_0 would be underestimated through N_0 , however, the diffusion coefficient from the transients would be still be expected to be reasonably accurate.

Conclusions

Gold deposition on silicon occurs through progressive nucleation of hemispherical clusters followed by diffusion limited 3D growth. The silicon/gold junction is rectifying and, hence, stripping cannot occur. Deposition takes place at sufficiently negative potentials such that the silicon surface is in accumulation. Hence, the applied potential is expected to be predominantly dropped across the Helmholtz layer, although a redistribution of the applied potential is expected upon deposition of gold. Analysis of the nucleation rate leads to a critical nucleus size of \leq two atoms suggesting that nucleus growth is dominated by the low probability of detachment (stripping). The nucleus densities obtained from surface imaging are much higher than values obtained from current transients, which may be related to the high nucleus densities found for this system. It is shown that models for nucleation and growth derived for metal-on-metal deposition can be applied to metal-on-semiconductor deposition if reduction occurs by charge transfer from the majority carrier band to the solution, and takes place at potentials where the semiconductor surface is in accumulation. In addition, the nucleation characteristics are strongly affected when deposition is an irreversible process.

Acknowledgments

The authors gratefully acknowledge support from the National Science Foundation under grant no. CTS-9732782.

The Johns Hopkins University assisted in meeting the publication costs of this article.

References

- P. Allongue and E. Souteyrand, *Electrochim. Acta*, **34**, 1027 (1989).
- P. Bindra, H. Gerischer, and D. M. Kolb, *J. Electrochem. Soc.*, **124**, 1012 (1977).
- Y. Nakato, K. Ueda, H. Yano, and H. Tsubomura, *J. Phys. Chem.*, **92**, 2316 (1988).
- G. Scherb and D. M. Kolb, *J. Electroanal. Chem.*, **396**, 151 (1995).
- P. M. Vereecken, K. Strubbe, and W. P. Gomes, *J. Electroanal. Chem.*, **433**, 19 (1997).
- R. M. Stiger, S. Gorer, B. Craft, and R. M. Penner, *Langmuir*, **15**, 790 (1999).
- G. Oskam, D. van Heerden, and P. C. Searson, *Appl. Phys. Lett.*, **73**, 3241 (1998).
- G. Oskam, J. G. Long, M. Nikolova, and P. C. Searson, in *Electrochemical Synthesis and Modification of Materials*, Mater. Res. Soc. Proc., Vol. 451, 257, MRS, Pittsburgh, PA (1997).
- G. Oskam, J. G. Long, A. Natarajan, and P. C. Searson, *J. Phys. D.: Appl. Phys.*, **31**, 1927 (1998).
- A. A. Pasa and W. Schwarzacher, *Phys. Status Solidi A*, **173**, 73 (1999).
- B. Rashkova, B. Guel, R. T. Pötzschke, G. Staikov, and W. J. Lorenz, *Electrochim. Acta*, **43**, 3021 (1998).
- P. Allongue, V. Costa-Kieling, and H. Gerischer, *J. Electrochem. Soc.*, **140**, 1009 (1993).
- P. Allongue, V. Costa-Kieling, and H. Gerischer, *J. Electrochem. Soc.*, **140**, 1021 (1993).
- O. J. Glembocki, R. E. Stahlbush, and M. Tomkiewicz, *J. Electrochem. Soc.*, **132**, 145 (1985).
- M. Beltowska-Brzezinska, E. Dutkiewicz, and W. Lawicki, *J. Electroanal. Chem.*, **99**, 341 (1979).
- E. T. Eisenmann, *J. Electrochem. Soc.*, **125**, 717 (1978).
- J. A. Harrison and J. Thompson, *J. Electroanal. Chem.*, **40**, 133 (1972).
- A. Natarajan, G. Oskam, and P. C. Searson, *J. Phys. Chem. B*, **102**, 7793 (1998).
- A. Natarajan, G. Oskam, and P. C. Searson, *J. Appl. Phys.*, **83**, 2112 (1998).
- G. Oskam, L. Bart, D. Vanmaekelbergh, and J. J. Kelly, *J. Appl. Phys.*, **74**, 3238 (1993).
- G. Oskam, D. Vanmaekelbergh, and J. J. Kelly, *Electrochim. Acta*, **38**, 1115 (1993).
- G. Oskam, J. C. Schmidt, P. M. Hoffmann, and P. C. Searson, *J. Electrochem. Soc.*, **143**, 2531 (1996).
- M. J. Madou, B. H. Loo, K. W. Frese, Jr., and S. R. Morrison, *Surf. Sci.*, **108**, 135 (1981).
- E. H. Roderick and R. H. Williams, *Metal-Semiconductor Contacts*, Oxford University Press, New York (1988).
- Southampton Electrochemistry Group, *Instrumental Methods in Electrochemistry*, Ellis Horwood, New York (1990).
- E. Budevski, G. Staikov, and W. J. Lorenz, *Electrochemical Phase Formation and Growth*, VCH, Weinheim (1996).
- G. Gunawardena, G. Hills, I. Montenegro, and B. Scharifker, *J. Electroanal. Chem.*, **138**, 225 (1982).
- G. Gunawardena, G. Hills, and I. Montenegro, *J. Electroanal. Chem.*, **138**, 241 (1982).
- B. R. Scharifker and G. J. Hills, *Electrochim. Acta*, **28**, 879 (1983).
- E. Bosco and S. K. Rangarajan, *J. Electroanal. Chem.*, **134**, 213 (1982).
- M. Y. Abyaneh, *Electrochim. Acta*, **27**, 1329 (1982).
- M. Sluyters-Rehbach, J. H. O. J. Wijenberg, E. Bosco, and J. H. Sluyters, *J. Electroanal. Chem.*, **236**, 1 (1987).
- E. B. Budevski, in *Comprehensive Treatise of Electrochemistry*, Vol. 7, B. E. Conway, J. O'M. Bockris, E. Yeager, S. U. M. Khan, and R. E. White, Editors, p. 399, Plenum Press, New York (1983).
- A. Milchev, *J. Electroanal. Chem.*, **457**, 47 (1998).
- I. Markov, A. Boynov, and S. Toshev, *Electrochim. Acta*, **18**, 377 (1973).
- A. Milchev, E. Vassileva, and V. Kertov, *J. Electroanal. Chem.*, **107**, 323 (1980).
- M. Volmer and A. Weber, *Z. Phys. Chem.*, **119**, 277 (1926).
- M. Volmer, *Kinetics of Phase Formation*, Steinkopff, Dresden (1939).
- R. Becker and W. Doering, *Ann. Phys. Leipzig*, **24**, 719 (1035).
- D. Walton, *J. Phys. Chem.*, **37**, 2182 (1962).
- D. Walton, in *Nucleation*, A. C. Zettlemoyer, Editor, Marcel Dekker, New York (1969).
- S. Stoyanov, in *Current Topics in Materials Science*, Vol. 3, E. Kaldis, Editor, North Holland, Amsterdam (1978).
- S. Stoyanov, *Thin Solid Films*, **18**, 91 (1973).
- A. Milchev and E. Vassileva, *J. Electroanal. Chem.*, **107**, 337 (1980).